Defect-Polaron and Enormous Light-Induced Fermi-level Shift at Halide Perovskite Surface

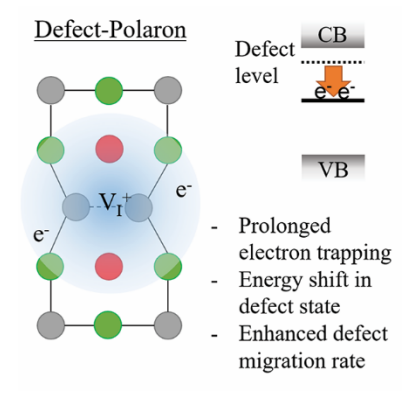
Ghadah Alkhalifah, ^{1,2} Angelo D. Marshall, ¹ Fatimah Rudayni, ^{1,3} Shanika Wanigasekara, ¹ Judy Z. Wu, ¹ Wai-Lun Chan^{1,*}

- 1. Department of Physics and Astronomy, University of Kansas, Lawrence, Kansas 66045, US
- 2. Department of Physics, College of Science, King Faisal University (KFU), Al-Ahsa 31982, Saudi Arabia
- 3. Department of Physics, Jazan University, Jazan 45142, Saudi Arabia

Abstract:

Halide perovskites intrinsically contain a large amount of point defects. The interaction of these defects with photocarriers, photons, and lattice distortion remains a complex and unresolved issue. We found that for halide perovskite films with excess halide vacancies, the Fermi level can be shifted by as much as 0.7 eV upon light illumination. These defects can trap photocarriers for hours after the light illumination is turned off. The enormous light-induced Fermi level shift and the prolonged electron trapping are explained by the capturing of photocarriers by halide vacancies at the surface of the perovskite film. The formation of this defect-photocarrier complex can result in lattice deformation and an energy shift in the defect state. The whole process is akin to polaron formation at a defect site. Our data also suggests that these trapped carriers increase the electrical polarizability of the lattice presumably by enhancing the defect migration rate.

*E-mail: wlchan@ku.edu



TOC Graphic

Organometal halide perovskites, such as methylammonium lead halide (MAPbI₃), have emerged as a leading contender for next generation photovoltaics (PV) applications. ¹⁻⁶ Free carriers in halide perovskites have a very long diffusion length ⁵⁻⁷ and a reasonably high mobility ⁸⁻¹⁰ despite they are synthesized using low-temperature processes that do not generally yield high quality crystals. Hence, how these imperfect materials can have such a high photo-to-electric conversion efficiency remains an intriguing question. Fundamentally, halide perovskites possess some interesting properties that are not typically found in other semiconductors. For example, halide perovskites have a soft and deformable lattice, which can interact with free carriers to form large polarons. ¹¹ The formation of polarons would minimize electron-phonon scattering, ¹²⁻¹³ and slow down hot electron cooling. ¹⁴⁻¹⁶ Moreover, although halide perovskite crystals often contain a high concentration of point defects, most of these defects only form shallow traps, ¹⁷⁻¹⁸ leaving a much reduced impact on free carrier mobility.

On the other hand, point defects or ionic defects in perovskites are also very mobile (e.g. the migration barrier for the Γ vacancy is only ~0.1 - 0.6 eV¹⁹⁻²²), which can result in a very large dielectric response.²³ Ionic defects diffusion and segregation²⁴⁻²⁸ have therefore presented a major challenge in practical applications. For instance, the interplay between defect diffusion and carrier trapping can lead to the infamous hysteresis found in current-voltage measurements.²⁹⁻³⁴ Moreover, the perovskite PVs are subjected to cyclic conditions such as the day/night³⁵ and the forward/reverse bias³⁶ cycles. Ionic defects can have reversible interactions with charges under these cyclic conditions, which makes the short-term performance highly depending on the precondition of the device. Depending on device architectures and perovskite film preparation methods, contradicting behaviors have been reported. For example, some studies reported that the PV efficiency degrades in the dark but recovers when it is exposed to light.³⁷ However, the exact

opposite behavior has been reported by others.^{35, 38} In fact, many of these non-intuitive behaviors still lack explanations. In order to have a better understanding and control of the device performance and stability, it is imperative to understand the complex interaction between electrons, defects, lattice deformation, and photons in the perovskite lattice.

Because ionic defects are charged particles, they can have strong interaction with free carriers. To further complicate the picture, it has been observed that the defect migration rate can be enhanced by orders of magnitude under light illumination, both in pristine peroskites^{21, 39} and in mixed halide perovskites.^{40,45} The mechanism underlying the light-enhanced defect migration is still under debate.²⁶ In particular, it is difficult to distinguish whether the enhanced diffusion is originated directly from the light-induced lattice distortion,⁴⁶ or indirectly from the interaction with photoexcited carriers.^{47,48} By doping MAPbI₃ with an electron acceptor phenyl-C61-butyric acid methyl ester (PCBM), we recently found that residual photocarriers alone (without the direct light exposure) is sufficient to enhance the ionic diffusion.⁴⁹ This previous work points to the importance of the interaction between photocarriers and ionic defect in controlling the defect migration and the electron transport. It has also been proposed that motions of electrons and ions can be coupled in halide perovskites.⁵⁰

In this work, we further investigate this defect-photocarrier interaction by intentionally increasing the concentration of point defects in the MAPbI₃ perovskite films. Interestingly, for films with excess iodide vacancies (V_I), we found that the Fermi level can be shifted by as much as 0.7 eV upon light illumination. Moreover, we found that the V_I defect switches to a deep electron trap when it captures photo-excited electrons. Photocarriers can be trapped for hours even after the light illumination is switched off. It is also found that these trapped carriers can make the lattice more electrically polarizable, presumably by assisting the defect migration. These observations are

explained by the interaction between ionic defects, lattice deformation, and photoexcited electrons. Specifically, we propose that a photoexcited electron can be captured readily by a V_I defect, which initiates the lattice deformation that in turn stabilizes the captured electron. The process is akin to polaron formation but occurs at a defect site. The enormous Fermi level shift (essentially changes the perovskite from n-doped to un-doped), prolonged electron trapping, and enhanced defect migration observed in our experiments can make the device performance heavily depends on its pre-condition especially when the device is operated under dark/light cycles.

Our proposed picture is based on some theoretical predictions, $^{51-56}$ which found that a V_I defect can be deformed into the so-called Pb-dimer when it captures an additional electron. We note that Pb-dimer formation in the bulk has been disputed as a computational artifact in some recent works in which a more accurate HSE06 hybrid functional with spin-orbit coupling (SOC) is used. $^{57-58}$ However, another computational work in which the HSE06+SOC is also employed has shown that Pb-dimer formation can be energetically feasible at surface or in regions where two V_I defects are clustered. 59 Furthermore, a recent simulation has shown that Pb-dimer at the surface can be further stabilized under light illumination when additional electrons in the conduction band can interact with the defect. 60 Because our main experimental technique, ultraviolet photoemission spectroscopy (UPS), is extremely surface sensitive (with a probe depth of ~ 1 nm or less), our experimental data appears to agree well with models that show Pb-dimer formation at the surface induced by electron trapping. $^{59-60}$

To introduce defects into the MAPbI₃ lattice, we varied the MAI:PbI₂ precursor ratio (*r*) from 0.8:1.2 to 1.2:0.8. Similar method has been employed by others to probe defect migration,⁶¹ and to determine the effect of ionic defects on doping⁶² and device performance.⁶³ Changing the precursor ratio by the aforementioned amount does not change the bandgap of MAPbI₃ or

significantly alter the film thickness, which we have verified experimentally (supporting information, Fig. S1 and S2). Scanning electron microscopy (SEM) images show that films made with these precursor ratios are continuous with similar morphologies (Fig. S3), except for the MAI-rich one (r = 1.2:0.8) in which some μ m-sized voids are observed. It is known that during the MAPbI₃ formation, adduct of PbI₂ is first formed because of its lower solubility. ⁶⁴⁻⁶⁵ Then, MA⁺ and Γ ions transform the PbI₂ into MAPbI₃. Hence, a MAI-deficient film (r < 1) likely contains iodide (V₁) and MA vacancies (V_{MA}), while a MAI-rich film (r > 1) likely contains iodide (I_i) and MA interstitials (MA_i). Indeed, those four kinds of defects are commonly observed in MAPbI₃⁶¹ while V₁ is often identified as the dominant defect species ⁶⁶ because of its low formation energy, the ready escape of Γ ions to environment νia I₂ formation, and its low migration energy.

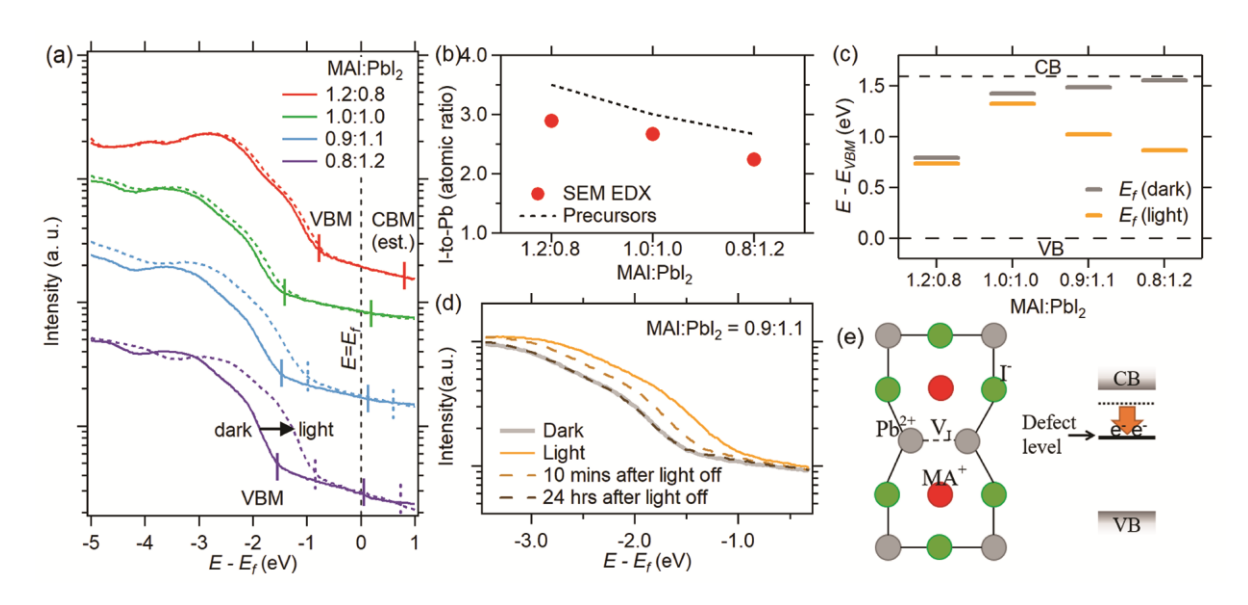


Figure 1: (a) The UPS spectra near the valence band maxima (VBM) region for perovskite films made with different precursor ratios. UPS spectra collected in dark and under light illumination are represented by solid and dashed lines, respectively. (b) The I:Pb ratio measured by SEM EDX (dots) and calculated from the precursor ratio (dashed line). (c) The position of the Fermi level (in dark and at light) for films with different precursor ratios. (d) Additional spectra for the 0.9:1.1 sample taken at 10 minutes and 24 hours after the light illumination is switched off. The result shows that the light-induced Fermi level shift is reversible after the light is switched off. (e) When the $V_{\rm I}$ defect captures an additional electron, a Pb-dimer can form. This lattice distortion can cause the defect level to shift towards the middle of the bandgap.

The type of the dominant defects in the perovskite can be determined using UPS⁶² in conjunction with energetic locations of defect levels calculated from first principle calculations. 17-¹⁸ Figure 1(a) shows the UPS spectra at the energy region near the valance band maxima (VBM) for perovskite films with different precursor ratios. Solid lines are spectra taken in the dark, and positions of the VBM are indicated on the figure. The energy is referenced with respect to the Fermi level (E_f) . The expected positions for the conduction band minimum (CBM) calculated using a bandgap of 1.59 eV are shown as vertical lines above the E_f . It can be seen that the MAI-deficient (r = 0.8:1.2) sample is highly n-doped while the MAI-rich sample (r = 1.2:0.8) sample is slightly p-doped. This data is consistent with previous UPS measurements on spin-coated MAPbI₃ films.⁶² It is known that the V_I defect has a defect level slightly below the CBM (a shallow electron trap). Hence, the n-doping of the MAI-deficient film can be associated with a large concentration of V_I defects. 17,62 We note that even the stoichiometric 1.0:1.0 film is n-doped, which is consistent with the consensus that V_I is the dominant defect in MAPbI₃.^{26, 66} For the MAI-rich film, the extra I⁻ ions can suppress the formation of V_I , which results in a E_f locating close to the middle of the band gap similar to that of an un-doped film. It has also been argued that MAI-rich samples contain Pbvacancies (V_{Pb}), which would explain the slightly p-doping observed in the MAI-rich sample. 17,62 Finally, the spectral shape of the valence band is essentially identical for all spectra. Hence, a common structural phase at the surface, which can be found in all MAI-deficient, stoichiometric, and MAI-rich films, is probed by the UPS. This common structural phase is much more likely to be MAPbI₃ instead of other phases such as un-transformed PbI₂ at grain boundaries that can only be found in MAI-deficient films.⁶⁷

The film stoichiometry is further verified by using energy dispersive X-ray (EDX) equipped in the SEM. The I:Pb ratio (atomic) of films made with different precursor ratios are

shown in Fig. 1b. The expected I:Pb ratio calculated using the precursor ratio is shown as the dashed line. While the data verifies that films with a lower MAI:PbI2 precursor ratio have a lower I:Pb ratio (i.e. more likely to contain V_I defects), ratios measured by the EDX are systematically lower than expected I:Pb ratios. It is known that iodine can be easily expulsed from the film, ^{39, 68} which can reduce the I:Pb ratio for all films. Indeed, our UPS measurement shows that the stoichiometric sample is n-doped, which indicates the presence of V_I. This agrees with the EDX measurement, which shows a I:Pb ratio less than 3 for the stoichiometric sample. Moreover, the absolute composition obtained by EDX would have a few percent error because the emitted X-ray intensity depends complicatedly on sample geometry and measurement condition, which would also contribute to the systematical error.

More interestingly, we observed that the E_f for MAI-deficient samples shifted significantly when the sample was illuminated by light. The UPS spectra taken under the illumination of a 532 nm continuous wave (CW) laser is shown as dashed lines in Fig. 1a. For MAI-deficient samples (purple lines), the Fermi level appears to shift significantly ($\sim 0.7 \text{ eV}$) towards the middle of the band gap under light. Under the same condition, only a small shift (< 0.1 eV) is observed for the stoichiometric (1.0:1.0) and the MAI-rich sample. For the two MAI-deficient samples (0.8:1.2 and 0.9:1.1), if we assume the Fermi level is pinned near the defect level, the average trap depth for the two samples increases from 0.08 eV (dark) to 0.65 eV (with light illumination). We note that the shift cannot be explained by the sample charging due to the photoemission process. These perovskite films are coated on a highly conductive indium tin oxide (ITO) substrate. Moreover, the electrical conductivity of the MAI-deficient sample (0.8:1.2) is at least an order of magnitude higher than that of the stoichiometric sample (1.0:1.0) (supporting information, Fig. S4). Hence, if the shift is originated from the sample charging because of a poor electrical conductivity, we

would have observed a similarly large shift in the 1.0:1.0 sample. Moreover, MAI-deficient films have similar microstructure as compared to the 1.0:1.0 film (Fig. S3). Indeed, it is the MAI-rich film that shows a different morphology and contain micro-sized pores. Therefore, the film morphology cannot explain why the abnormal behavior is observed in MAI-deficient films, but not MAI-rich films. The positions of the Fermi level for all samples under dark and light conditions are summarized in Fig. 1c. The light intensity used is ~ 81 mW/cm², which is close to the solar irradiance (~100 mW/cm²). Hence, the observation is relevant to typical solar cell operation conditions.

The light-induced shift in the Fermi level is reversible. Figure 1d shows two additional spectra for the 0.9:1.1 sample collected after the laser was switched off. Ten minutes after the laser was switched off, the Fermi level shifts halfway back to the original position. The position of the Fermi level restores back to the original position after the sample was kept in dark overnight. The reversibility indicates that the Fermi level shift is not caused by light-induced damages. As we will show, MAI-deficient films can also trap electrons for a prolonged period. To understand whether the light-induced Fermi level shift is caused by trapped electrons alone, or by the interaction between trapped electrons and the defective perovskite lattice, we perform a control experiment with a stoichiometric (1.0:1.0) film mixed with ~ 1 % PCBM. It is known that the PCBM molecules cluster at grain boundaries of perovskite films.⁶⁹⁻⁷⁰ Our previous work has shown that the PCBM in MAPbI₃ can trap a large amount of electrons, ⁷¹ similar to the electron trapping behavior found in the MAI-deficient film (see below). Despite the stoichiometric film with 1% PCBM can also trap electrons, it does not show any light-induced Fermi level shift behavior (supporting information Fig. S5). Hence, the shift is produced by the interaction between trapped electrons with the defective perovskite lattice. The MAI-deficient samples are expected to have a large

amount of V_I defects. Therefore, we hypothesize that the shift is originated from the interaction of V_I defect with excited electrons created by the optical excitation. In the discussion below, we will focus on the MAI-deficient film which shows the strong light-induced effect and presumably have a high concentration of V_I defects.

Theoretical studies⁵¹⁻⁵³ have shown that when the V_I has a charge state of 0 (i.e. a single electron is bound by the positive V_I defect), the defect level is slightly below the CBM which corresponds to a shallow electron trap. However, if the defect captures an additional electron (the charge state changes to -1), the lattice deforms and a Pb dimer is formed (Fig. 1e). The lattice deformation lowers the energy of the defect level, which results in the formation of a deep electron trap. 51-53 The additional electron can be originated from optical excitation, 53 which can explain the observed light-induced effect in MAI-deficient samples. Although some recent simulation works that employ more accurate functional have discarded Pb dimer formation in the bulk as a computational artifect, 57-58 Pb dimer formation is still energetically feasible near the surface or around clustered V_I defects. ⁵⁹ Since defects tend to cluster at grain boundaries, Pb dimer formation would be feasible at grain boundaries as well. Because the UPS is a surface sensitive technique, the light-induced Fermi-level shift we observed is consistent with the Pb-dimer formation at the surface. Another recent theoretical work shows that additional electrons in the conduction band can stabilize the Pb-dimer, 60 which means that Pb-dimer formation can be induced by light illumination as observed in our experiment. Because the whole process resembles polaron formation at an ionic defect site, we will refer this defect complex to as a "defect-polaron". For a doped semiconductor, the E_f is located at the highest occupied gap state. Hence, the formation of the defect-polaron causes the shift of the E_f towards the middle of the bandgap, which agrees well with our UPS measurements.

Finally, other defects such as I-interstitial can also trap electrons and undergo a similar defect-polaron formation process.⁵⁷ However, I-interstitials are more likely to be found in iodiderich films and create p-doping. By contrast, our MAI-deficient films are n-doped (from UPS) and iodide-deficient (from EDX). Other point defect species including MA-interstitial, Pb-interstitial, MAI (MA ion at the I-site), PbI, and PbMA can produce n-doping.⁷² However, MA-interstitial is not likely to be the dominant type of defects in a MAI-deficient film. Pb-interstitial, MAI, PbI, and PbMA have large defect formation energies (> 1 eV),⁷² and to our knowledge, they have not been commonly considered as the dominant defect in halide perovskite films.

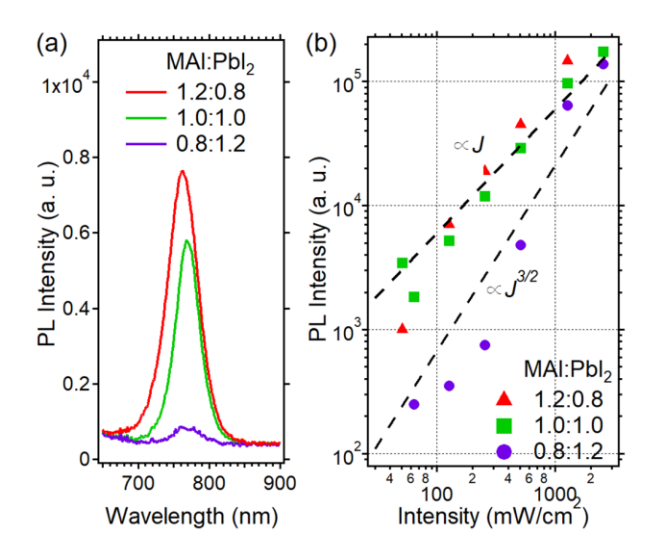


Figure 2: (a) The PL spectra for perovskite films with different precursor ratios. The intensity of the excitation source is $\sim 120 \text{ mW/cm}^2$. For the MAI-deficient film, the PL intensity is quenched. (b) The PL intensity as a function of the intensity of the excitation source shown on a log-log plot. The data collected from the MAI-deficient sample shows a different slope (n = 3/2) than that of the stoichiometric sample (n = 1). The dependence supports electron trapping is a dominant decay channel in the MAI-deficient sample.

The photoexcited electron is essentially trapped by the V_I because a significant amount of energy will be required to ionize the electron from the defect level to the conduction band once the defect-polaron is formed. Hence, formation of the defect-polaron state should reduce the radiative recombination of free electron-hole pairs. We measure the photoluminescence (PL)

intensity of our samples by pumping the sample with the 532 nm-CW laser. Figure 2a shows a comparison of the PL spectra collected from the 0.8:1.2, 1.0:1.0, and 1.2:0.8 samples at a pump laser intensity of ~120 mW/cm². A PL peak at ~ 770 nm, which corresponds to the radiative recombination of a free electron-hole pair, can be observed in all samples. However, the MAI-deficient sample (0.8:1.2) shows an order of magnitude weaker PL intensity. The observed PL quenching is consistent with the proposed electron trapping mechanism because trapped electrons are likely to recombine through other non-radiative recombination channels instead of re-exciting back to the conduction band for radiative recombination to occur.

To verify our defect-polaron hypothesis, we further measured how the PL intensity depends on the pump laser intensity. We note that light fluence dependences have often been used to understand photocarrier recombination and trapping mechanisms.⁷³⁻⁷⁴ The intensity dependences are shown in Fig. 2b. The PL intensity changes much more dramatically with the laser intensity for the MAI-deficient sample (purple) as compared to other samples. The dependence of the radiative recombination yield Y on the laser intensity J under different dominant relaxation channels can be derived using a simple rate equation model, which is described in the Supporting Information. In short, we note that if bimolecular recombination is the main decay channel for free carriers, the product of the steady-state concentrations of free electron and hole concentration ($n \times 1$) p) should be proportional to I. The radiative recombination yield Y, which is also a bimolecular process, should be proportional to $n \times p$ and hence, J. The $Y \propto I$ dependence matches well with results from the 1.0:1.0 and the 1.2:0.8 samples (see the n = 1 curve in Fig. 2b). On the other hand, if defect-mediated trapping is the dominant relaxation channel for free electrons, n is proportional to J (the derivation is provided in Supporting Information). As a result, the dependence between Y and J becomes $Y \propto I^{3/2}$. Indeed, for the MAI-deficient sample (0.8:1.2), the result fits well with

the $Y \propto J^{3/2}$ relationship. This shows that electron trapping is the dominant relaxation channel in the MAI-deficient sample, which is consistent with our proposed defect-polaron mechanism.

To verify the existence of these deep electron traps, the perovskite film is spin-coated on a graphene field effect transistor (GFET). Unlike metals, graphene has an extremely low density of states (DOS) near the Dirac point. Hence, even a small doping would cause a significant shift in the E_f , which makes graphene an extremely sensitive charge sensor. At the perovskite/graphene heterostructure, even a small charge imbalance in the perovskite layer can induce charge doping in graphene via capacitive coupling. When light excites the perovskite, it creates electron-hole pairs. Previously, our group^{71,76} and others^{77,79} have found that electrons are preferentially trapped in the perovskite, while holes are injected readily into graphene. Although the selective electron trapping was often simply attributed to the band bending near the graphene-perovskite interface without independent evidences, the stoichiometry-dependent measurement presented below suggests that V_I defects can play an important role in facilitating such selective electron trapping.

The polarity of charges trapped in the perovskite when the film is illuminated by light can be determined using a back-gated sample as shown schematically in Fig. 3a. By applying a back gate voltage (V_g) to the SiO₂/Si back gate, the graphene can be doped electrically.⁸⁰ For the r = 1.0:1.0 sample, the source-drain current (I_{sd}) is measured as a function of back-gate voltage (V_g). The result is shown in Fig. 3b. The measurement is done in the dark and in the presence of white light illumination (intensity ~ 0.13 mW/cm²). The whole curve shifts to the positive V_g direction (blue arrow) after the light exposure. This result indicates that light illumination creates a steady-state population of net negative charges in the perovskite. Because only electrons/holes, but not ionic charges, can leave the perovskite and inject into the graphene, the net negative charge in perovskite can be attributed to the selective electron trapping in the perovskite.

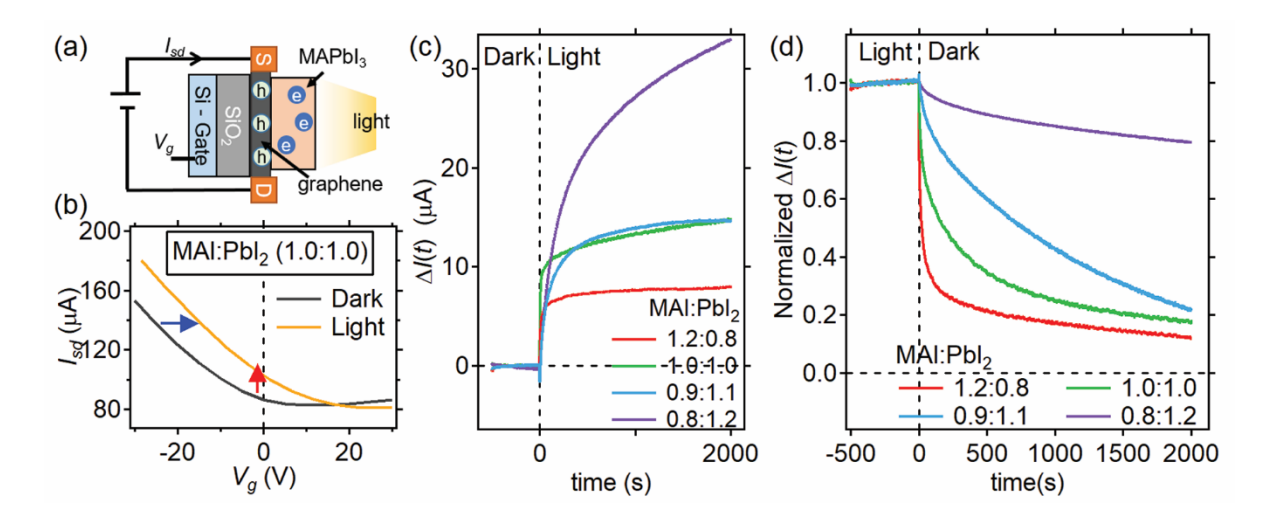


Figure 3. (a) A Schematic diagram showing the principle of the GFET measurement. Charges trapped in the perovskite film induce an equal number (but with an opposite polarity) of doped charges in graphene, which causes a change in the graphene's conductivity. (b) The source-drain current (I_{sd}) versus the back gate voltage (V_g) for the 1.0:1.0 sample kept in dark (black) and at light (orange). The curve shifts to the positive V_g direction (blue arrow), which indicates electron trapping in perovskite. Note that at $V_g = 0$, light causes an increase in I_{sd} (red arrow). (c) The temporal dynamics of the light-induced change of I_{sd} (ΔI_{sd}) at $V_g = 0$ when samples are exposed to light. The light is switched on at t = 0 s. (d) The normalized ΔI_{sd} when the light is switched off. Data from MAI-deficient samples shows a much larger decay time constant, which shows that these samples contain deep electron traps. For all these measurements, a white light source with an intensity of 0.13 mW/cm² was used.

To determine the extent and the dynamics of the electron trapping, we kept $V_g = 0$ and measured the temporal evolution of the I_{sd} after the same white light was switched on/off. As shown in Fig. 3b, the I_{sd} increases under light at $V_g = 0$ (red arrow). The temporal dynamics of this photo-induced change in the source-drain current (ΔI_{sd}) is shown in Fig. 3c. In this plot, the light is switched on at t = 0. The MAI-rich sample (1.2:0.8) shows the weakest signal increase while the MAI-deficient sample (0.8:1.2) shows the strongest increase. All samples (including those MAI-rich ones) show light-induced electron trapping behavior. However, the MAI deficiency samples show a larger signal compared to the MAI-rich ones, which can be explained by the active electron trapping by V_I defects and a larger V_I concentration in MAI-deficient films. We have also probed the decay dynamics of the ΔI_{ds} after the light is switched off (Fig. 3d). To compare the decay

dynamics, the signal is normalized with the ΔI_{ds} at t=0. Interestingly, the MAI-rich film shows much a faster response as compared to the MAI-deficient film. For the 0.8:1.2 film, the I_{sd} typically takes ~ 10 hours to restore its dark value. The signal decay time for the 0.8:1.2 sample is at least 2 orders of magnitude larger than that of the 1.2:0.8 sample. The result agrees with our hypothesis that V_I defects in the MAI-deficient sample are deep traps for photoexcited electrons. These deep electron traps allow photoexcited electrons to remain in the perovskite film for hours even after the light is switched off.

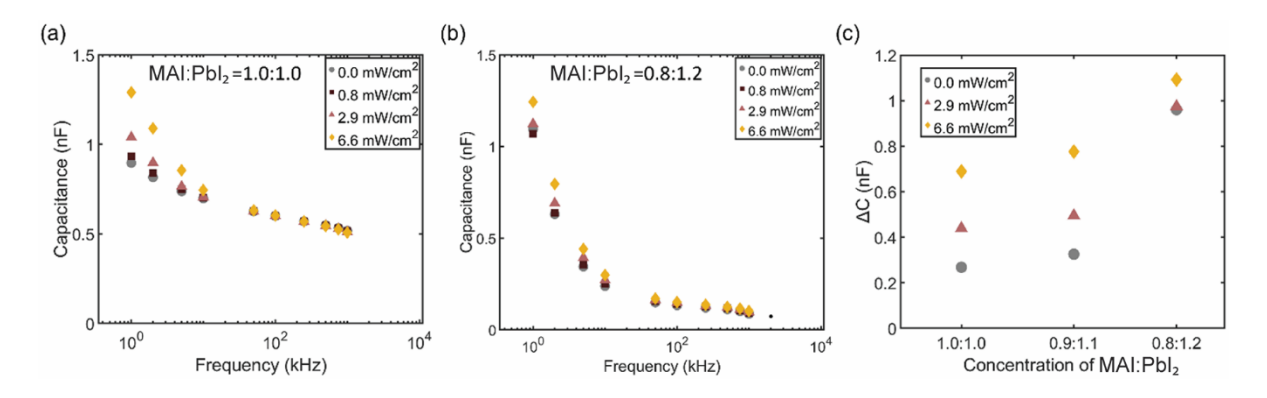


Figure 4: Capacitance versus frequency at different light intensities for the a) MAI:PbI₂ = 1.0:1.0, and b) MAI:PbI₂ = 0.8:1.2 samples. (c) The increase in capacitance, $\Delta C = C(100 \text{ kHz}) - C(1 \text{kHz})$ for various light intensities versus the precursor ratio. Light illumination results in a larger ΔC because defect migration is enhanced when the sample is exposed to light. For the MAI deficient film (0.8:1.2), ΔC remains large even after the light is turned off (0 mW/cm²), which shows that the presence of trapped electrons in perovskites can enhance the defect migration as well.

In our recent work, ⁴⁹ we have found that the presence of residual photocarriers trapped in the perovskite can enhance the defect migration as well. In the case of the V_I defect, an electron captured by the V_I significantly lowers the energy of the Pb-dimer configuration, which would lower the energy barrier for the V_I migration.⁵³ To probe the ionic defect migration, we measure the frequency-dependent dielectric response using an Al/perovskite/florine-doped tin oxide (FTO) capacitor structure.⁴⁹ In this measurement, an ac voltage with frequencies in the range of 1 kHz to 1 MHz was applied across the two electrodes of the capacitor. The polarization in the perovskite

layer induced by the ac electric field is reflected in an increase in the ac capacitance.^{66, 81} Figures 4a and b show the frequency dependence of the capacitance for the stoichiometric (1.0:1.0) and the MAI-deficient (0.8:1.2) sample at different light intensities. A significant uptake in the capacitance (hence, the dielectric constant) is observed at frequencies < 100 kHz, which has often been attributed to the electrical polarization contributed by the migration of V_I defects.⁶⁶ The extent of the capacitance increase can be further enhanced by the light illumination (yellow symbols in Fig. 4a), which has been attributed to the light-enhanced ion migration found in MAPbI₃.^{66, 81}

To probe the effect of trapped carriers on the defect migration, we lowered the light intensity step-by-step, and the dark measurement (grey circles) was taken within a few minutes after the light was fully turned off. For the MAI-deficient sample, because electrons can be trapped for a few hours in the perovskite after the light was turned off (Fig. 3d), the effect of trapped electrons on the defect migration can be probed. For the MAI-deficient sample, the capacitance only decreases slightly after the light is turned off (Fig. 4b). Hence, trapped electrons appear to play a similar role as light (photocarriers) in enhancing the defect migration. To compare the capacitance change, Fig. 4c plots the quantity $\Delta C = C (1 \text{ kHz}) - C (100 \text{ kHz})$ for the two compositions at different light illumination conditions. We attribute this capacitance difference to the increase in the electrical polarization induced by the defect migration when the ionic defect begins to respond to the ac E-field at low frequencies (< 100 kHz). For the MAI-deficient sample (0.8:1.2), ΔC remains large for both light and dark measurements (i.e. defect migration remains fast even after the light was switched off). By contrast, for the 1.0:1.0 sample, ΔC becomes much smaller when the sample was in dark. Similar behaviors is previously observed in perovskite films doped with PCBM. 49 PCBM is a well-known electron acceptor. When mixed into the perovskite

film, the PCBM domains act as deep electron traps. In our previous work on PCBM, we argued that residue holes in perovskite created by the charge separation between perovskite and PCBM can assist the ion migration even after the light illumination is switched off. The similarity of the frequency-dependent capacitance observed in the MAI-deficient sample and the PCBM-doped sample further verifies our hypothesis that the trapped electron can assist the migration of the $V_{\rm I}$ defect.

Finally, we note that holes can also interact with defects to induce lattice distortion, which in turn enhance the defect migration rate. For example, a recent work has shown that holes trapped in perovskites can speed up the migration of iodide ions. ⁸² A subsequent simulation work shows that photoexcited holes can be trapped by the V_I, which results in lattice distortion. ⁸³ The process is similar to the Pb-dimer formation discussed here, but the distortion around the defect site has a different geometry. These previous works and our current work show that the soft nature of the perovskite lattice can generally lead to lattice distortion when charges are trapped at defect sites. This can in turn lower the defect migration barrier and enhance its migration rate.

In summary, our photoemission spectroscopy, PL spectroscopy, charge trapping, and dielectric response measurements have collectively shown that MAI-deficient samples exhibit more severe electron trapping effect than the stochiometric 1.0:1.0 or the MAI-rich samples. Interestingly, the MAI-deficient sample shows a large and reversible shift in the Fermi level when it is exposed to light. We attribute the observed Fermi level shift to the capturing of the photoexcited electron by the V_I defect at the perovskite surface. Our experimental finding agrees well with some previous theoretical models, 51-53, 59-60 which have shown that the capturing additional electrons by the V_I defect can cause lattice deformation (Pb-dimer formation). This deformation in turn shifts the defect level from the edge of the conduction band towards the middle

of the bandgap, which changes V_I from a shallow electron trap to a deep electron trap. Our results not only verify this theoretical prediction, but also reveal some important consequences of this light induced trapping mechanism via the formation of defect-polarons. First, the formation of defect-polarons causes an enormous shift in the Fermi level, which can result in a light-induced band bending near interfaces formed by the perovskite and other materials. Second, photoexcited electrons can turn V_I defects into deep photocarrier traps which can trap photoexcited electrons inside the perovskites for hours even after the light illumination is turned off. Because trapped electrons take hours to dissipate, the mechanism can potentially explain various light soaking behaviors observed in perovskite devices. Therefore, the defect-lattice-photocarrier interaction must be considered for understanding the performance stability of perovskite devices under cyclic operation conditions.

Experimental Method

Perovskite films fabrication: Perovskite films were coated on indium tin oxide (ITO), glass, and fluorine-doped tin oxide (FTO) substrates for the UPS, PL spectroscopy, and the capacitor measurements, respectively. All these substrates were cleaned by soaking in detergent for 10 minutes. Then, they were sonicated in acetone and isopropyl alcohol (10 minutes for each solvent). The substrates were then treated by ozone for 15 min before the perovskite deposition.

The perovskite precursor solution was prepared by dissolving lead iodide (Alfa Aesar, 99.9985%) and methylammonium iodide (Luminescence Technology, 99.5%) with varying stoichiometry in N,N-dimethylformamide (DMF, ACROS organics, 99.8%). The stoichiometric sample (1.0:1.0) was prepared with a solution concentration of 0.75 M. For other molar ratios (MAI:PbI₂ varied from 0.8:1.2 to 1.2:0.8), the concentrations for MAI and PbI₂ were varied accordingly. The solution was heated at 70 °C and stirred overnight. Then, the perovskite solution

was spin-coated on the substrate at room temperature in a nitrogen-filled glovebox at 3000 rpm for 30 s and then 6000 rpm for 3 s. An antisolvent, chlorobenzene (Macron), was dropped onto the film during spin coating process. The prepared samples were annealed at 60 °C for 5 min, 80 °C for 5 min, and 100 °C for 10 min to remove the residual solvent. The samples were cooled down inside the N₂ glovebox before being taken out.

Perovskite films fabricated on FTO were used for capacitance measurement. For these samples, Al (30 nm) top electrodes were deposited on the MAPbI₃ using DC magnetron sputtering through a shadow mask with multiple circular holes to define the diameter of the capacitor to be $494\pm8~\mu m$ with a total capacitor area of $\sim1.9-2.0\times10^5~\mu m^2$. The deposition rate of Al was calibrated to be 0.54~nm/second.

GFET devices fabrication: CVD-grown monolayer graphene (purchased from graphene supermarket) was transferred onto SiO₂(300 nm)/Si substrates by the standard wet-PMMA transfer method. Copper electrodes with a thickness of 100nm were deposited on the transferred graphene using sputter deposition through a shadow mask. Graphene channels (1 mm \times 1 mm) were patterned using another shadow mask with an Ar ion beam. Then, the graphene was annealed in a UHV chamber (base pressure $\sim 1 \times 10^{-9}$) at 400 °C overnight. In order to fabricate perovskite films with grain size and thickness similar to those fabricated on ITO, slightly different spin coating parameters were used. The perovskite solution and graphene substrate were preheated on a hotplate (80 °C) prior to spin coating. The solution was spin-coated on the graphene at 500 rpm for 30 s, and then at 3000 rpm for 60 s. An antisolvent (isopropyl alcohol) was dropped onto the film during the spin coating. The film was annealed at 80 °C for 20 min, and at 100 °C for 10 min.

<u>Ultraviolet photoemission spectroscopy (UPS)</u>: UPS was carried out in a home-built ultrahigh vacuum (UHV) chamber, with a base pressure of $< 1 \times 10^{-10}$ Torr, equipped with a

hemispherical energy analyzer (SPECS, Phoibos 100). The He-I emission line (21.2 eV) was used in this experiment. The sample was biased at -2 V during the UPS experiment. A 532 nm continuous wave (CW) laser was used to illuminate the sample. A collimated beam was used so that the whole sample was illuminated by the laser.

Absorption and photoluminescence (PL) spectroscopy: The optical absorption spectra were collected using a home-built setup consisting of a tungsten-halogen light source (Thorlabs SLS201L) and a StellarNet BLUE-Wave spectrometer. The PL spectra were measured by the spectrometer and the sample was excited by a 532 nm CW laser.

Graphene device measurement: The perovskite/graphene device was mounted in a high vacuum cryostat and the sample was kept in dark overnight before measurement. A tungsten-halogen light source (Thorlabs SLS201L) was used for light illumination. During the measurement, a source-drain voltage of 0.5 V was applied. The current was measured by a Keysight 34450A digital multimeter. For some measurements, a back gate voltage was applied.

<u>Capacitance measurement</u>: The capacitance-voltage (C-V) measurements were done using tungsten probes (Lakeshore) in a high vacuum probe station (base pressure $\sim 1 \times 10^{-6}$ Torr). An Agilent semiconductor analyzer B1505A was employed for the C-V characteristic measurements. Our device can be modeled as a RC circuit consisting of a capacitor connected in parallel with a resistor of large resistance across the vertical direction through the film thickness. ⁶⁶ The presence of the resistance (real part of the impedance) would not prevent the ability to determine the capacitance (imaginary part of the impedance) because both quantities can be extracted from the ac measurement of the circuit impedance. A Schott 20500 ACE 1 Fiber Optic Illuminator light source with controlled intensity of 0, 0.6, 2.9 and 6.6 mW/cm² was used to measure the light-induced change in the capacitance. For all measurements, a low applied DC bias voltage of 100

mV was selected to prevent dielectric breakdown of the perovskite thin film capacitors. An a.c. voltage (amplitude = 100 mV) with frequencies in the range of 1 kHz to 1 MHz was applied across the two electrodes. For the dark and light measurements, data was taken within 5 - 10 minutes after the light was turned off and on.

SUPPORTING INFORMATION

Optical absorption spectra, film thickness measurements, SEM images of the films, electrical conductivity measurements, additional UPS spectra, and the model for fitting the light-intensity dependence of the PL data.

ACKNOWLEDGEMENT

W. -L. C. acknowledges the support by US National Science Foundation grants DMR-2109979 and the support by the University of Kansas General Research Fund allocation #2151080. W.-L. C. also like to thank Junliang Yang for some helpful discussion on the Pb-Pb dimer formation mechanism. A.M. and J.Z.W acknowledge US National Science Foundation grants DMR-1909292 and ECCS-1809293. G.A. acknowledges the support provided by the Deanship of Scientific Research, Vice Presidency for Graduate Studies and Scientific Research, King Faisal University, Saudi Arabia [GRANT319]. F.R. acknowledges the scholarship support from Jazan University.

References:

- (1) Conings, B.; Baeten, L.; De Dobbelaere, C.; D'Haen, J.; Manca, J.; Boyen, H. G. Perovskite-Based Hybrid Solar Cells Exceeding 10% Efficiency with High Reproducibility Using a Thin Film Sandwich Approach. *Adv. Mater.* **2014**, *26*, 2041-2046.
- (2) Green, M. A.; Ho-Baillie, A.; Snaith, H. J. The emergence of perovskite solar cells. *Nat. Photon.* **2014**, *8*, 506-514.
- (3) Eperon, G. E.; Stranks, S. D.; Menelaou, C.; Johnston, M. B.; Herz, L. M.; Snaith, H. J. Formamidinium lead trihalide: a broadly tunable perovskite for efficient planar heterojunction solar cells. *Energy Environ Sci* **2014**, *7*, 982-988.
- (4) Mosconi, E.; Amat, A.; Nazeeruddin, M. K.; Gratzel, M.; De Angelis, F. First-Principles Modeling of Mixed Halide Organometal Perovskites for Photovoltaic Applications. *J. Phys. Chem. C* **2013**, *117*, 13902-13913.
- (5) Xing, G. C.; Mathews, N.; Sun, S. Y.; Lim, S. S.; Lam, Y. M.; Gratzel, M.; Mhaisalkar, S.; Sum, T. C. Long-Range Balanced Electron- and Hole-Transport Lengths in Organic-Inorganic CH3NH3PbI3. *Science* **2013**, *342*, 344-347.
- (6) Stranks, S. D.; Eperon, G. E.; Grancini, G.; Menelaou, C.; Alcocer, M. J. P.; Leijtens, T.; Herz, L. M.; Petrozza, A.; Snaith, H. J. Electron-Hole Diffusion Lengths Exceeding 1 Micrometer in an Organometal Trihalide Perovskite Absorber. *Science* **2013**, *342*, 341-344.

- (7) Dong, Q. F.; Fang, Y. J.; Shao, Y. C.; Mulligan, P.; Qiu, J.; Cao, L.; Huang, J. S. Electron-hole diffusion lengths > 175 mu m in solution-grown CH3NH3PbI3 single crystals. *Science* **2015**, *347*, 967-970.
- (8) Chen, Y.; Yi, H. T.; Wu, X.; Haroldson, R.; Gartstein, Y. N.; Rodionov, Y. I.; Tikhonov, K. S.; Zakhidov, A.; Zhu, X. Y.; Podzorov, V. Extended carrier lifetimes and diffusion in hybrid perovskites revealed by Hall effect and photoconductivity measurements. *Nat. Commun.* **2016,** 7, 12253.
- (9) Wehrenfennig, C.; Eperon, G. E.; Johnston, M. B.; Snaith, H. J.; Herz, L. M. High Charge Carrier Mobilities and Lifetimes in Organolead Trihalide Perovskites. *Adv. Mater.* **2014**, *26*, 1584-1589.
- (10) Ponseca, C. S.; Savenije, T. J.; Abdellah, M.; Zheng, K. B.; Yartsev, A.; Pascher, T.; Harlang, T.; Chabera, P.; Pullerits, T.; Stepanov, A.; Wolf, J. P.; Sundstrom, V. Organometal Halide Perovskite Solar Cell Materials Rationalized: Ultrafast Charge Generation, High and Microsecond-Long Balanced Mobilities, and Slow Recombination. *J. Am. Chem. Soc.* **2014**, *136*, 5189-5192.
- (11) Zhu, H. M.; Miyata, K.; Fu, Y. P.; Wang, J.; Joshi, P. P.; Niesner, D.; Williams, K. W.; Jin, S.; Zhu, X. Y. Screening in crystalline liquids protects energetic carriers in hybrid perovskites. *Science* **2016**, *353*, 1409-1413.
- (12) Zhu, X. Y.; Podzorov, V. Charge Carriers in Hybrid Organic-Inorganic Lead Halide Perovskites Might Be Protected as Large Polarons. *J. Phys. Chem. Lett.* **2015**, *6*, 4758-4761.
- (13) Brenner, T. M.; Egger, D. A.; Rappe, A. M.; Kronik, L.; Hodes, G.; Cahen, D. Are Mobilities in Hybrid Organic-Inorganic Halide Perovskites Actually "High"? *J. Phys. Chem. Lett.* **2015**, *6*, 4754-4757.
- (14) Frost, J. M.; Whalley, L. D.; Walsh, A. Slow Cooling of Hot Polarons in Halide Perovskite Solar Cells. *ACS Energy Lett.* **2017**, *2*, 2647-2652.
- (15) Bretschneider, S. A.; Ivanov, I.; Wang, H. I.; Miyata, K.; Zhu, X. Y.; Bonn, M. Quantifying Polaron Formation and Charge Carrier Cooling in Lead-Iodide Perovskites. *Adv. Mater.* **2018**, *30*, 1707312.
- (16) Guo, Z.; Wan, Y.; Yang, M. J.; Snaider, J.; Zhu, K.; Huang, L. B. Long-range hot-carrier transport in hybrid perovskites visualized by ultrafast microscopy. *Science* **2017**, *356*, 59-62.
- (17) Yin, W. J.; Shi, T. T.; Yan, Y. F. Unusual defect physics in CH3NH3PbI3 perovskite solar cell absorber. *Appl. Phys. Lett.* **2014**, *104*, 063903.
- (18) Kim, J.; Lee, S. H.; Lee, J. H.; Hong, K. H. The Role of Intrinsic Defects in Methylammonium Lead Iodide Perovskite. *J. Phys. Chem. Lett.* **2014**, *5*, 1312-1317.
- (19) Eames, C.; Frost, J. M.; Barnes, P. R. F.; O'Regan, B. C.; Walsh, A.; Islam, M. S. Ionic transport in hybrid lead iodide perovskite solar cells. *Nat. Commun.* **2015**, *6*, 7497.
- (20) Senocrate, A.; Moudrakovski, I.; Kim, G. Y.; Yang, T. Y.; Gregori, G.; Gratzel, M.; Maier, J. The Nature of Ion Conduction in Methylammonium Lead Iodide: A Multimethod Approach. *Angew Chem. Int. Ed.* **2017**, *56*, 7755-7759.
- (21) Xing, J.; Wang, Q.; Dong, Q. F.; Yuan, Y. B.; Fanga, Y. J.; Huang, J. S. Ultrafast ion migration in hybrid perovskite polycrystalline thin films under light and suppression in single crystals. *PCCP* **2016**, *18*, 30484-30490.
- (22) Li, C.; Guerrero, A.; Zhong, Y.; Huettner, S. Origins and mechanisms of hysteresis in organometal halide perovskites. *J. Phys.: Condens. Matter* **2017**, *29*, 193001.

- (23) Juarez-Perez, E. J.; Sanchez, R. S.; Badia, L.; Garcia-Belmonte, G.; Kang, Y. S.; Mora-Sero, I.; Bisquert, J. Photoinduced Giant Dielectric Constant in Lead Halide Perovskite Solar Cells. *J. Phys. Chem. Lett.* **2014**, *5*, 2390-2394.
- (24) Xiao, Z. G.; Yuan, Y. B.; Shao, Y. C.; Wang, Q.; Dong, Q. F.; Bi, C.; Sharma, P.; Gruverman, A.; Huang, J. S. Giant switchable photovoltaic effect in organometal trihalide perovskite devices. *Nat. Mater.* **2015**, *14*, 193-198.
- (25) Tress, W. Metal Halide Perovskites as Mixed Electronic-Ionic Conductors: Challenges and Opportunities-From Hysteresis to Memristivity. *J. Phys. Chem. Lett.* **2017**, *8*, 3106-3114.
- (26) Walsh, A.; Stranks, S. D. Taking Control of Ion Transport in Halide Perovskite Solar Cells. *ACS Energy Letters* **2018**, *3*, 1983-1990.
- (27) Egger, D. A.; Rappe, A. M.; Kronik, L. Hybrid Organic-Inorganic Perovskites on the Move. *Acc. Chem. Res.* **2016**, *49*, 573-581.
- (28) Zhao, Y.; Liang, C. J.; Zhang, H. M.; Li, D.; Tian, D.; Li, G. B.; Jing, X. P.; Zhang, W. G.; Xiao, W. K.; Liu, Q.; Zhang, F. J.; He, Z. Q. Anomalously large interface charge in polarity-switchable photovoltaic devices: an indication of mobile ions in organic-inorganic halide perovskites. *Energy Environ Sci* **2015**, *8*, 1256-1260.
- (29) van Reenen, S.; Kemerink, M.; Snaith, H. J. Modeling Anomalous Hysteresis in Perovskite Solar Cells. *J. Phys. Chem. Lett.* **2015**, *6*, 3808-3814.
- (30) Unger, E. L.; Hoke, E. T.; Bailie, C. D.; Nguyen, W. H.; Bowring, A. R.; Heumuller, T.; Christoforo, M. G.; McGehee, M. D. Hysteresis and transient behavior in current-voltage measurements of hybrid-perovskite absorber solar cells. *Energy Environ Sci* **2014**, *7*, 3690-3698.
- (31) Shao, Y. H.; Xiao, Z. G.; Bi, C.; Yuan, Y. B.; Huang, J. S. Origin and elimination of photocurrent hysteresis by fullerene passivation in CH3NH3PbI3 planar heterojunction solar cells. *Nat. Commun.* **2014**, *5*, 5784.
- (32) Snaith, H. J.; Abate, A.; Ball, J. M.; Eperon, G. E.; Leijtens, T.; Noel, N. K.; Stranks, S. D.; Wang, J. T. W.; Wojciechowski, K.; Zhang, W. Anomalous Hysteresis in Perovskite Solar Cells. *J. Phys. Chem. Lett.* **2014**, *5*, 1511-1515.
- (33) Egger, D. A.; Edri, E.; Cahen, D.; Hodes, G. Perovskite Solar Cells: Do We Know What We Do Not Know? *J. Phys. Chem. Lett.* **2015**, *6*, 279-282.
- (34) Chen, B.; Yang, M. J.; Priya, S.; Zhu, K. Origin of J-V Hysteresis in Perovskite Solar Cells. *J. Phys. Chem. Lett.* **2016,** *7*, 905-917.
- (35) Domanski, K.; Roose, B.; Matsui, T.; Saliba, M.; Turren-Cruz, S. H.; Correa-Baena, J. P.; Carmona, C. R.; Richardson, G.; Foster, J. M.; De Angelis, F.; Ball, J. M.; Petrozza, A.; Mine, N.; Nazeeruddin, M. K.; Tress, W.; Gratzel, M.; Steiner, U.; Hagfeldt, A.; Abate, A. Migration of cations induces reversible performance losses over day/night cycling in perovskite solar cells. *Energy Environ Sci* **2017**, *10*, 604-613.
- (36) Bowring, A. R.; Bertoluzzi, L.; O'Regan, B. C.; McGehee, M. D. Reverse Bias Behavior of Halide Perovskite Solar Cells. *Adv Energy Mater* **2018**, *8*, 1702365.
- (37) Huang, F. Z.; Jiang, L. C.; Pascoe, A. R.; Yan, Y. F.; Bach, U.; Spiccia, L.; Cheng, Y. B. Fatigue behavior of planar CH3NH3PbI3 perovskite solar cells revealed by light onioff diurnal cycling. *Nano Energy* **2016**, *27*, 509-514.
- (38) Nie, W.; Blancon, J. C.; Neukirch, A. J.; Appavoo, K.; Tsai, H.; Chhowalla, M.; Alam, M. A.; Sfeir, M. Y.; Katan, C.; Even, J.; Tretiak, S.; Crochet, J. J.; Gupta, G.; Mohite, A. D. Light-activated photocurrent degradation and self-healing in perovskite solar cells. *Nat. Commun.* **2016**, *7*, 11574.

- (39) Kim, G. Y.; Senocrate, A.; Yang, T. Y.; Gregori, G.; Gratzel, M.; Maier, J. Large tunable photoeffect on ion conduction in halide perovskites and implications for photodecomposition. *Nat Mater* **2018**, *17*, 445-449.
- (40) Barker, A. J.; Sadhanala, A.; Deschler, F.; Gandini, M.; Senanayak, S. P.; Pearce, P. M.; Mosconi, E.; Pearson, A. J.; Wu, Y.; Kandada, A. R. S.; Leijtens, T.; De Angelis, F.; Dutton, S. E.; Petrozza, A.; Friend, R. H. Defect-Assisted Photoinduced Halide Segregation in Mixed-Halide Perovskite Thin Films. *ACS Energy Lett.* **2017**, *2*, 1416-1424.
- (41) Hoke, E. T.; Slotcavage, D. J.; Dohner, E. R.; Bowring, A. R.; Karunadasa, H. I.; McGehee, M. D. Reversible photo-induced trap formation in mixed-halide hybrid perovskites for photovoltaics. *Chem Sci* **2015**, *6*, 613-617.
- (42) Yoon, S. J.; Draguta, S.; Manser, J. S.; Sharia, O.; Schneider, W. F.; Kuno, M.; Kamat, P. V. Tracking Iodide and Bromide Ion Segregation in Mixed Halide Lead Perovskites during Photoirradiation. *ACS Energy Lett.* **2016**, *1*, 290-296.
- (43) Zhang, H. C.; Fu, X.; Tang, Y.; Wang, H.; Zhang, C. F.; Yu, W. W.; Wang, X. Y.; Zhang, Y.; Xiao, M. Phase segregation due to ion migration in all-inorganic mixed-halide perovskite nanocrystals. *Nat. Commun.* **2019**, *10*, 1088.
- (44) Draguta, S.; Sharia, O.; Yoon, S. J.; Brennan, M. C.; Morozov, Y. V.; Manser, J. M.; Kamat, P. V.; Schneider, W. F.; Kuno, M. Rationalizing the light-induced phase separation of mixed halide organic-inorganic perovskites. *Nat. Commun.* **2017**, *8*, 200.
- (45) Brennan, M. C.; Draguta, S.; Kamat, P. V.; Kuno, M. Light-Induced Anion Phase Segregation in Mixed Halide Perovskites. *ACS Energy Lett.* **2018**, *3*, 204-213.
- (46) Tsai, H.; Asadpour, R.; Blancon, J. C.; Stoumpos, C. C.; Durand, O.; Strzalka, J. W.; Chen, B.; Verduzco, R.; Ajayan, P. M.; Tretiak, S.; Even, J.; Alam, M. A.; Kanatzidis, M. G.; Nie, W.; Mohite, A. D. Light-induced lattice expansion leads to high -efficiency perovskite solar cells. *Science* **2018**, *360*, 67-70.
- (47) Egger, D. A.; Kronik, L.; Rappe, A. M. Theory of Hydrogen Migration in Organic-Inorganic Halide Perovskites. *Angew Chem. Int. Ed.* **2015**, *54*, 12437-12441.
- (48) Whalley, L. D.; Crespo-Otero, R.; Walsh, A. H-Center and V-Center Defects in Hybrid Halide Perovskites. *ACS Energy Lett.* **2017**, *2*, 2713-2714.
- (49) Marshall, A. D.; Acharya, J.; Alkhalifah, G.; Kattel, B.; Chan, W. L.; Wu, J. Z. Probing the Origin of Light-Enhanced Ion Diffusion in Halide Perovskites. *ACS Appl. Mater. Inter.* **2021**, *13*, 33609-33617.
- (50) Kerner, R. A.; Rand, B. P. Ionic-Electronic Ambipolar Transport in Metal Halide Perovskites: Can Electronic Conductivity Limit Ionic Diffusion? *J. Phys. Chem. Lett.* **2018**, *9*, 132-137.
- (51) Agiorgousis, M. L.; Sun, Y. Y.; Zeng, H.; Zhang, S. B. Strong Covalency-Induced Recombination Centers in Perovskite Solar Cell Material CH(3)NH(3)Pbl(3). *J. Am. Chem. Soc.* **2014**, *136*, 14570-14575.
- (52) Tong, C. J.; Li, L. Q.; Liu, L. M.; Prezhdo, O. V. Synergy between Ion Migration and Charge Carrier Recombination in Metal-Halide Perovskites. *J. Am. Chem. Soc.* **2020**, *142*, 3060-3068.
- (53) Wang, J.; Duan, X. M.; Yin, W. J. Photoinduced Dynamic Defects Responsible for the Giant, Reversible, and Bidirectional Light-Soaking Effect in Perovskite Solar Cells. *J. Phys. Chem. Lett.* **2021**, *12*, 9328-9335.

- (54) Wang, J.; Li, W.; Yin, W. J. Passivating Detrimental DX Centers in CH3NH3PbI3 for Reducing Nonradiative Recombination and Elongating Carrier Lifetime. *Adv. Mater.* **2020**, *32*, 1906115.
- (55) Zhang, Z. S.; Qiao, L.; Mora-Perez, C.; Long, R.; Prezhdo, O. V. Pb dimerization greatly accelerates charge losses in MAPbI(3): Time-domain ab initio analysis. *J. Chem. Phys.* **2020**, *152*, 064707.
- (56) Li, W.; Sun, Y. Y.; Li, L. Q.; Zhou, Z. H.; Tang, J. F.; Prezhdo, O. V. Control of Charge Recombination in Perovskites by Oxidation State of Halide Vacancy. *J. Am. Chem. Soc.* **2018**, *140*, 15753-15763.
- (57) Meggiolaro, D.; De Angelis, F. First-Principles Modeling of Defects in Lead Halide Perovskites: Best Practices and Open Issues. *ACS Energy Lett.* **2018**, *3*, 2206-2222.
- (58) Kang, J. Effects of band edge positions on defect structure in lead halide perovskites: A case study on the Br vacancy in CsPbBr3. *Phys Rev Mater* **2020**, *4*, 085405.
- (59) Zhang, L. H.; Sit, P. H. L. Ab initio study of the dynamics of electron trapping and detrapping processes in the CH3NH3PbI3 perovskite. *J Mater Chem A* **2019**, *7*, 2135-2147.
- (60) Feng, X. X.; Liu, B.; Peng, Y. Y.; Gu, C. X.; Bai, X.; Long, M. Q.; Cai, M. Q.; Tong, C. J.; Han, L. Y.; Yang, J. L. Restricting the Formation of Pb-Pb Dimer via Surface Pb Site Passivation for Enhancing the Light Stability of Perovskite. *Small* **2022**, *18*, 2201831.
- (61) Reichert, S.; An, Q. Z.; Woo, Y. W.; Walsh, A.; Vaynzof, Y.; Deibel, C. Probing the ionic defect landscape in halide perovskite solar cells. *Nat. Commun.* **2020**, *11*, 6098.
- (62) Wang, Q.; Shao, Y. C.; Xie, H. P.; Lyu, L.; Liu, X. L.; Gao, Y. L.; Huang, J. S. Qualifying composition dependent p and n self-doping in CH3NH3PbI3. *Appl. Phys. Lett.* **2014**, *105*, 163508.
- (63) Fassl, P.; Lami, V.; Bausch, A.; Wang, Z. P.; Klug, M. T.; Snaith, H. J.; Vaynzof, Y. Fractional deviations in precursor stoichiometry dictate the properties, performance and stability of perovskite photovoltaic devices. *Energy Environ Sci* **2018**, *11*, 3380-3391.
- (64) Ahn, N.; Son, D. Y.; Jang, I. H.; Kang, S. M.; Choi, M.; Park, N. G. Highly Reproducible Perovskite Solar Cells with Average Efficiency of 18.3% and Best Efficiency of 19.7% Fabricated via Lewis Base Adduct of Lead(II) Iodide. *J. Am. Chem. Soc.* **2015**, *137*, 8696-8699.
- (65) Li, B.; Binks, D.; Cao, G. Z.; Tian, J. J. Engineering Halide Perovskite Crystals through Precursor Chemistry. *Small* **2019**, *15*, 1903613.
- (66) Wang, H. X.; Guerrero, A.; Bou, A.; Al-Mayouf, A. M.; Bisquert, J. Kinetic and material properties of interfaces governing slow response and long timescale phenomena in perovskite solar cells. *Energy Environ Sci* **2019**, *12*, 2054-2079.
- (67) Meier, T.; Gujar, T. P.; Schonleber, A.; Olthof, S.; Meerholz, K.; van Smaalen, S.; Panzer, F.; Thelakkat, M.; Kohler, A. Impact of excess PbI2 on the structure and the temperature dependent optical properties of methylammonium lead iodide perovskites. *J. Mater. Chem. C* **2018**, *6*, 7512-7519.
- (68) Mathew, P. S.; Samu, G. F.; Janaky, C.; Kamat, P. V. Iodine (I) Expulsion at Photoirradiated Mixed Halide Perovskite Interface. Should I Stay or Should I Go? *ACS Energy Lett.* **2020**, *5*, 1872-1880.
- (69) Xu, J.; Buin, A.; Ip, A. H.; Li, W.; Voznyy, O.; Comin, R.; Yuan, M. J.; Jeon, S.; Ning, Z. J.; McDowell, J. J.; Kanjanaboos, P.; Sun, J. P.; Lan, X. Z.; Quan, L. N.; Kim, D. H.; Hill, I. G.; Maksymovych, P.; Sargent, E. H. Perovskite-fullerene hybrid materials suppress hysteresis in planar diodes. *Nat. Commun.* **2015**, *6*, 7081.

- (70) Chiang, C. H.; Wu, C. G. Bulk heterojunction perovskite-PCBM solar cells with high fill factor. *Nat. Photon.* **2016**, *10*, 196-200.
- (71) Qin, L.; Wu, L. P.; Kattel, B.; Li, C. H.; Zhang, Y.; Hou, Y. B.; Wu, J.; Chan, W. L. Using Bulk Heterojunctions and Selective Electron Trapping to Enhance the Responsivity of Perovskite-Graphene Photodetectors. *Adv. Funct. Mater.* **2017**, *27*, 1704173.
- (72) Ran, C. X.; Xu, J. T.; Gao, W. Y.; Huang, C. M.; Dou, S. X. Defects in metal triiodide perovskite materials towards high-performance solar cells: origin, impact, characterization, and engineering. *Chem. Soc. Rev.* **2018**, *47*, 4581-4610.
- (73) Saba, M.; Cadelano, M.; Marongiu, D.; Chen, F. P.; Sarritzu, V.; Sestu, N.; Figus, C.; Aresti, M.; Piras, R.; Lehmann, A. G.; Cannas, C.; Musinu, A.; Quochi, F.; Mura, A.; Bongiovanni, G. Correlated electron-hole plasma in organometal perovskites. *Nat. Commun.* **2014**, *5*, 5049.
- (74) Draguta, S.; Thakur, S.; Morozov, Y. V.; Wang, Y. X.; Manser, J. S.; Kamat, P. V.; Kuno, M. Spatially Non-uniform Trap State Densities in Solution-Processed Hybrid Perovskite Thin Films. *J. Phys. Chem. Lett.* **2016**, *7*, 715-721.
- (75) Castro Neto, A. H.; Guinea, F.; Peres, N. M. R.; Novoselov, K. S.; Geim, A. K. The electronic properties of graphene. *Rev. Mod. Phys.* **2009**, *81*, 109-162.
- (76) Wu, L. P.; Qin, L.; Zhang, Y.; Alamri, M.; Gong, M. G.; Zhang, W.; Zhang, D.; Chan, W. L.; Wu, J. Z. High-Sensitivity Light Detection via Gate Tuning of Organometallic Perovskite/PCBM Bulk Heterojunctions on Ferroelectric Pb0.92La0.08Zr0.52Ti0.48O3 Gated Graphene Field Effect Transistors. *ACS Appl. Mater. Inter.* **2018**, *10*, 12824-12830.
- (77) Spina, M.; Lehmann, M.; Nafradi, B.; Bernard, L.; Bonvin, E.; Gaal, R.; Magrez, A.; Forro, L.; Horvath, E. Microengineered CH3NH3PbI3 Nanowire/Graphene Phototransistor for Low-Intensity Light Detection at Room Temperature. *Small* **2015**, *11*, 4824-4828.
- (78) Lee, Y.; Kwon, J.; Hwang, E.; Ra, C. H.; Yoo, W. J.; Ahn, J. H.; Park, J. H.; Cho, J. H. High-Performance Perovskite-Graphene Hybrid Photodetector. *Adv. Mater.* **2015**, *27*, 41-46.
- (79) Wang, Y.; Zhang, Y.; Lu, Y.; Xu, W.; Mu, H.; Chen, C.; Qiao, H.; Song, J.; Li, S.; Sun, B.; Cheng, Y.-B.; Bao, Q. Hybrid Graphene–Perovskite Phototransistors with Ultrahigh Responsivity and Gain. *Advanced Optical Materials* **2015**, *3*, 1389-1396.
- (80) Zhang, Y. B.; Tang, T. T.; Girit, C.; Hao, Z.; Martin, M. C.; Zettl, A.; Crommie, M. F.; Shen, Y. R.; Wang, F. Direct observation of a widely tunable bandgap in bilayer graphene. *Nature* **2009**, *459*, 820-823.
- (81) Zarazua, I.; Bisquert, J.; Garcia-Belmonte, G. Light-Induced Space-Charge Accumulation Zone as Photovoltaic Mechanism in Perovskite Solar Cells. *J. Phys. Chem. Lett.* **2016,** *7*, 525-528.
- (82) DuBose, J. T.; Mathew, P. S.; Cho, J. S.; Kuno, M.; Kamat, P. V. Modulation of Photoinduced Iodine Expulsion in Mixed Halide Perovskites with Electrochemical Bias. *J. Phys. Chem. Lett.* **2021**, *12*, 2615-2621.
- (83) Tong, C. J.; Cai, X. Y.; Zhu, A. Y.; Liu, L. M.; Prezhdo, O. V. How Hole Injection Accelerates Both Ion Migration and Nonradiative Recombination in Metal Halide Perovskites. *J. Am. Chem. Soc.* **2022**, *144*, 6604-6612.
- (84) Qin, L.; Kattel, B.; Kafle, T. R.; Alamri, M.; Gong, M.; Panth, M.; Hou, Y.; Wu, J.; Chan, W. L. Scalable Graphene-on-Organometal Halide Perovskite Heterostructure Fabricated by Dry Transfer. *Adv. Mater. Interfaces* **2019**, *6*, 1801419.